


Monitoring of compound resting membrane potentials of cell cultures with ratiometric genetically encoded voltage indicators

Philipp Rühl¹, Johanna M. Langner¹, Jasmin Reidel¹, Roland Schönherr¹, Toshinori Hoshi² & Stefan H. Heinemann¹  ¹✉

The cellular resting membrane potential (V_m) not only determines electrical responsiveness of excitable cells but also plays pivotal roles in non-excitable cells, mediating membrane transport, cell-cycle progression, and tumorigenesis. Studying these processes requires estimation of V_m , ideally over long periods of time. Here, we introduce two ratiometric genetically encoded V_m indicators, rArc and rASAP, and imaging and analysis procedures for measuring differences in average resting V_m between cell groups. We investigated the influence of ectopic expression of K^+ channels and their disease-causing mutations involved in Andersen-Tawil (Kir2.1) and Temple-Baraitser ($K_v10.1$) syndrome on median resting V_m of HEK293T cells. Real-time long-term monitoring of V_m changes allowed to estimate a 40–50 min latency from induction of transcription to functional Kir2.1 channels in HEK293T cells. The presented methodology is readily implemented with standard fluorescence microscopes and offers deeper insights into the role of the resting V_m in health and disease.

¹Center for Molecular Biomedicine, Department of Biophysics, Friedrich Schiller University Jena and Jena University Hospital, D-07745 Jena, Germany.

²Department of Physiology, University of Pennsylvania, Philadelphia, PA, USA. ✉email: Stefan.H.Heinemann@uni-jena.de

The cell membrane potential (V_m) and its changes are key to cellular excitability and many other physiological/pathophysiological processes, such as membrane transport, cell-cycle progression, embryonic development, and cancer, contributing to the overall driving force on other ions and solutes^{1–8}. Knowing resting V_m is therefore essential for understanding the underlying mechanisms.

Resting V_m is typically measured with electrophysiological methods, such as sharp microelectrodes or whole-cell patch clamp. However, the necessity to approach single cells with one electrode at a time renders these methods tedious and time consuming. Furthermore, disturbing the cell's integrity by rupturing the membrane and replacing the intracellular medium with a predefined pipette solution, as in the whole-cell patch-clamp method, severely limit the applicability of electrode-based methods for comparing V_m of different populations of cells. Much less invasive are voltage-sensitive organic dyes such as Di-4-ANEPPS, or FRET-oxonol systems, which have been used to study changes in V_m for decades^{9–11}. However, these organic dyes have notable drawbacks: limitations in the targeting to specific cell populations, the need of carefully optimized loading procedures, potential cytotoxicity, or direct interference with ion transport proteins^{11,12}. Some of these limitations are minimized in genetically encoded voltage indicators (GEVIs).

The potentiometric GEVIs ArcLight, ASAP, and more recently developed derivatives, based on voltage-sensitive phosphatases of, e.g., *Ciona intestinalis* or *Gallus gallus*, feature bright fluorescence and a large dependence of fluorescence intensity on V_m changes^{13–16}. Archaelhodopsin-based sensors are fast and have a large dynamic range but typically suffer from low quantum yields^{17,18}. Newly developed GEVIs are usually optimized for the detection of fast changes in V_m , such as neuronal action potentials¹⁹. Only a small fraction of research has focused on calibrating the signals with respect to the absolute V_m ^{20,21}. However, changes of V_m on time scales of minutes to days elicited by altered activity and/or expression of ion channels, electrogenic transporters, and pumps are proposed to occur during cell-cycle and tumor progression¹. The investigation of such processes therefore requires GEVIs that report resting V_m differences between cell populations or changes over extended periods of time.

For monitoring V_m , existing techniques suffer from various technical limitations and application hurdles. Determination of the absolute V_m with the nonequilibrium dynamics of a rhodopsin photocycle requires a time-resolved, multiwavelength pump-probe protocol²¹. The voltage-dependent signals arising from two GEVIs, ASAP1 and CAESR, were analyzed with fluorescence lifetime imaging microscopy (FLIM) to estimate absolute V_m ²⁰. However, FLIM needs a high-speed dedicated and specialized setup that may not be readily available in many physiology and biology laboratories, thus limiting the widespread adoption. Although measurement of resting V_m with ratiometric GEVIs was suggested earlier²², to our knowledge it has not been attempted with any of the currently available ratiometric GEVIs such as VSFP2.42 or Mermaid2^{17,23–26}.

Here, we exploited the large dynamic range of the potentiometric GEVI families ArcLight and ASAP, and developed *ratiometric* variants based on ArcLight-Q239 (rArc) and ASAP2s (rASAP). Although none of the developed indicators offered single-cell V_m accuracy, we successfully deployed them in microscopy-based procedures for automated extraction of fluorescence information from high numbers of cells (>1000) to compare compound resting V_m of independent cell groups. The easy-to-implement experimental strategy of standard fluorescence microscopic image acquisition and analysis, as outlined below, enabled us to evaluate the impact of the expression of disease-relevant ion channels and channel mutants on resting V_m of large populations of cells in

culture. Furthermore, long-term live-cell imaging allowed to estimate the biogenesis speed of Kir2.1 channels from triggered transactivation to functional channels in real time.

Results

Comparison of ratiometric GEVIs based on ArcLight and ASAP. We generated ratiometric GEVIs by fusing the red fluorescent protein mKate2 to the N terminus of the potentiometric GEVI ArcLight-Q239 (Fig. 1a, here termed rArc) or to ASAP2s with point mutations I67T and Q397R (Fig. 1b, here termed rASAP)^{13,14,27,28}. In addition, we constructed a rASAP variant in which the linker between the transmembrane segment S3 of the voltage-sensitive phosphatase and cpGFP (Fig. 1b) was altered (rASAP-al) according to the mutations in ASAP3¹⁶.

The three GEVIs, rArc, rASAP and rASAP-al, produced robust fluorescence signals in HEK293T cells. The red fluorescence signals (F_{red}) of all three GEVIs were independent of V_m when controlled by whole-cell patch clamp (Fig. 1c, d). The ratio of green to red fluorescence (F_{green}/F_{red}) of rASAP was smaller than that of rArc or rASAP-al at the same V_m (Fig. 1e, f) owing to relatively dimmer F_{green} . For all GEVIs, F_{green} underwent rapid and saturable loss after the start of illumination caused by reversible photoswitching (Supplementary Fig. 1a, b), as reported previously for other ASAP variants²⁹. In contrast to F_{green} , F_{red} originating from mKate2 was stable during illumination (Supplementary Fig. 1c). To acquire images after the F_{green} signal stabilized, simultaneous patch-clamp and imaging experiments were performed according to the recording protocol shown in Supplementary Fig. 1d. Furthermore, residual photobleaching was compensated (Supplementary Fig. 1e). The resulting $F_{green}/F_{red}(V_m)$ followed a Boltzmann-type function (Eq. 1) with maximum change, midpoint voltage, and slope factor (Δr , V_{half} , k_s) of 41%, -49 mV, 27.8 mV for rArc, 63%, 11.4 mV, -53.8 mV for rASAP, and 60%, -19 mV, 36.7 mV for rASAP-al (Fig. 1e, f and Supplementary Table 1). We excluded rASAP-al from further investigation because its sensitivity optimum ($V_{half} \pm k_s$) was in a voltage range unsuitable for faithful determination of average resting V_m , which is typically between 0 and -100 mV¹.

Voltage-step-induced F_{green} changes of rArc and rASAP followed a double-exponential time course with fast and slow components (Supplementary Fig. 2a). For a voltage step from -140 to 60 mV, a fast component time constant of 7.2 ± 0.3 ms with a relative amplitude (a_{fast}) of $70.2 \pm 1.4\%$ and a slow component time constant of 73 ± 5 ms was determined for rASAP. For rArc, both, the fast (18.7 ± 1.1 ms, $65.4 \pm 1.4\%$) and slow components (158 ± 14 ms) were substantially slower than for rASAP (Supplementary Fig. 2b, c).

We also designed ArcLight-Q239 fusion constructs based on the red fluorescent protein mCherry (rArc-mCherry). However, F_{red} images showed bright intracellular punctuate structures (Supplementary Fig. 3a), as reported previously for the FRET-based GEVIs Mermaid1 and Mermaid2²⁶. Similar punctuate structures are found with some of the DsRed-derived fluorescence proteins and were reported to originate from insufficient lysosomal fluorescence protein degradation³⁰. Variant rArc-mCherry-M71T, which shifts the pK_a of mCherry from less than 4 to 7.8³¹, mitigated the formation of bright F_{red} spots (Supplementary Fig. 3a) probably because of the acidic endosomal pH. However, the mutation also decreased the intensity of the red signal by about sevenfold and substantially increased the cell-to-cell variation in the F_{green}/F_{red} signal compared to rArc-mCherry and rArc (Supplementary Fig. 3b–d). While bright intracellular structures, which are likely caused by GEVI located in ER and Golgi, were also visible for all other GEVIs, we did not observe these punctuate red fluorescent structures for mKate2-based rArc (Supplementary Fig. 3a).

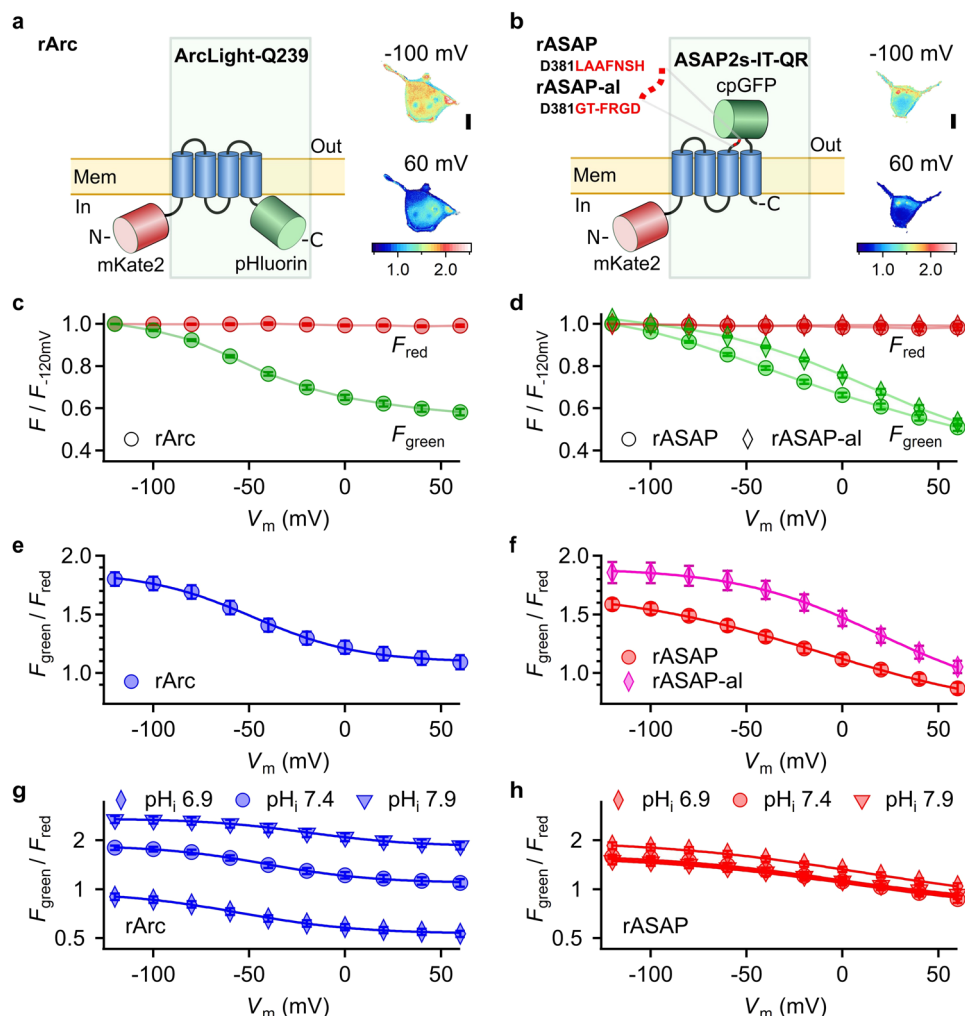


Fig. 1 Evaluation of ratiometric GEVIs based on ArcLight and ASAP. **a, b** Schematics of ratiometric rArcLight-Q239 (rArc) and ratiometric ASAP2s-I67T-Q397R (rASAP). rASAP and rASAP-al differ in the linker between the S3 transmembrane segment of the voltage-sensitive phosphatase and cpGFP as indicated. Pixel-by-pixel fluorescence ratio ($F_{\text{green}}/F_{\text{red}}$) images of HEK293T cells expressing rArc (**a**) or rASAP (**b**) voltage-clamped to the indicated V_m . Images were acquired with 470 nm (green) and 530 nm (red) excitation light (Supplementary Fig. 1). Calibration bar indicates $F_{\text{green}}/F_{\text{red}}$ values. Scale bar, 10 μm . **c, d** Normalized F_{green} and F_{red} signals of voltage-clamped cells with rArc, rASAP, or rASAP-al; $n = 10\text{--}11$. Straight lines connect data points for clarity. **e, f** $F_{\text{green}}/F_{\text{red}}$ from fluorescence data shown in (**c**) and (**d**) as a function of V_m . The $F_{\text{green}}/F_{\text{red}}$ signal was corrected for bleaching (Supplementary Fig. 1). Regions of interests (ROIs) for data extraction included the membrane areas only. **g, h** $F_{\text{green}}/F_{\text{red}}$ as a function of voltage of cells expressing rArc or rASAP with intracellular solution adjusted to the indicated intracellular pH (pH_i). Data at $\text{pH}_i 7.4$ are identical to data in (**e**) and (**f**), respectively; $n = 7\text{--}11$. Data are means \pm sem. Smooth curves in **e-h** are the results of fits according to Eq. 1; for results see Supplementary Table 1.

In live-cell imaging experiments the extracellular pH is determined by the choice of the bath solution, while the intracellular pH (pH_i) is not directly controlled. Since ArcLight-Q239 is based on the fluorescent protein pHluorin whose strong pH sensitivity is critical for the high Δr value of ArcLight-Q239^{31,32}, we investigated the impact of pH_i variations on $F_{\text{green}}/F_{\text{red}}(V_m)$ of rArc and rASAP. $F_{\text{green}}/F_{\text{red}}(V_m)$ of rArc was particularly sensitive to pH_i changes: at -100 mV, $F_{\text{green}}/F_{\text{red}}$ at $\text{pH}_i 7.9$ was threefold larger than at $\text{pH}_i 6.9$ (Fig. 1g and Supplementary Table 1); this difference was greater than any measured $F_{\text{green}}/F_{\text{red}}$ change caused by manipulation of V_m at a constant pH_i . In contrast, alteration of pH_i had only a minor impact on $F_{\text{green}}/F_{\text{red}}(V_m)$ of rASAP (Fig. 1h).

Live-cell high-content assay for detecting changes in compound resting V_m . One of the greatest advantages of optical V_m monitoring methods over those using electrodes is the possibility to record from thousands of cells simultaneously. We developed a

high-content, microscopy-based measurement technique that allowed us to automatically extract the F_{green} and F_{red} signals of cells. HEK293T cells were treated with the blue fluorescent membrane-permeable DNA dye Hoechst 33342³³, which highlights the cell nucleus and enables automatic generation of regions of interest (ROIs) using a thresholding procedure and a subsequent particle analysis algorithm (Fig. 2a). This method of ROI selection not only allows for automation but also minimizes the contribution of GEVI fluorescence from intracellular organelles because the cytosolic space above and below the nucleus is quite limited (Fig. 2a). In this way we acquired and automatically analyzed $F_{\text{green}}/F_{\text{red}}$ data from 10,000–60,000 cells per culture dish (Fig. 2b). Non-transfected and low-expressing cells as well as cells with very large fluorescence were eliminated by setting cutoffs based on F_{red} (Fig. 2b). Although both rArc and rASAP showed a relatively large cell-to-cell variation in $F_{\text{green}}/F_{\text{red}}$ (Fig. 2c, d), the median of the $F_{\text{green}}/F_{\text{red}}$ distribution proved to be a robust data descriptor: for example, for only 1000 cells the estimated standard deviation of the median, based on resampling of the cell-to-cell

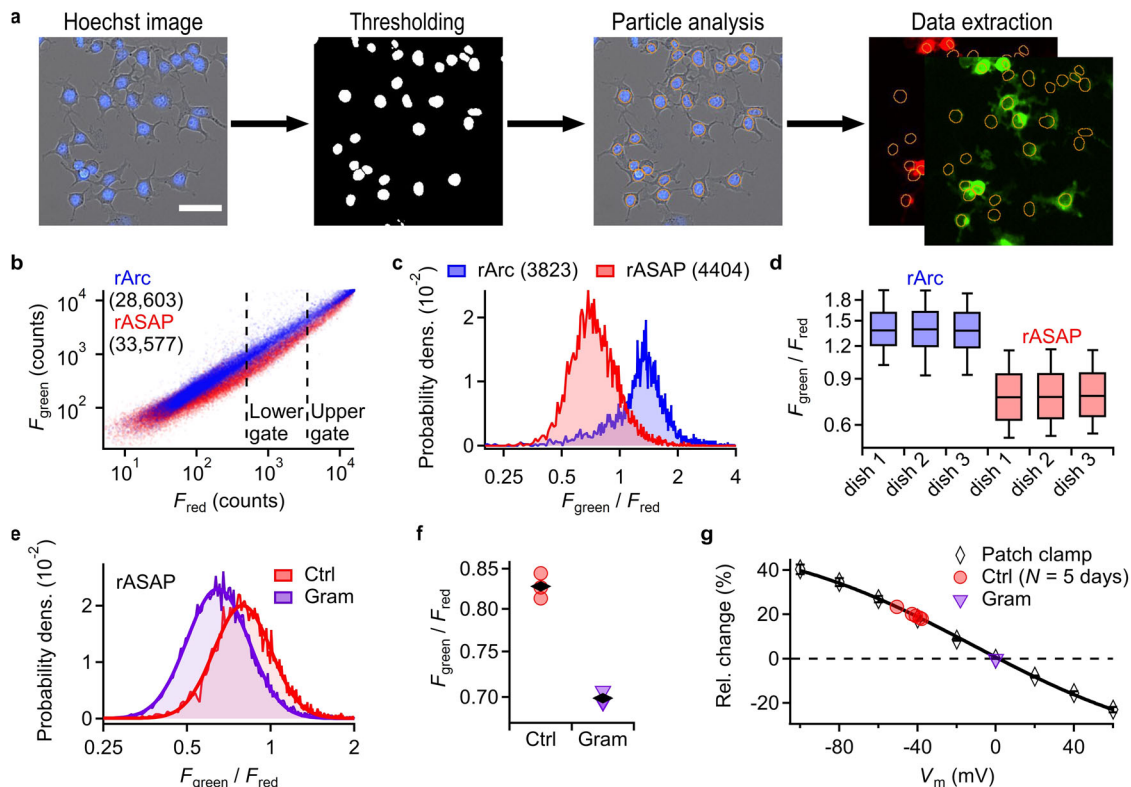


Fig. 2 Automated high-content assay. **a** Workflow for automated extraction of fluorescence information from images of plated HEK293T cells expressing ratiometric GEVIs; cells were pretreated with the DNA-binding dye Hoechst 33342 enabling automated ROI (orange circles) generation by setting a fluorescent threshold and applying a particle analysis algorithm on the F_{blue} channel. F_{blue} and transmission light images are superimposed. Scale bar, 50 μm . For details see methods. **b** F_{green} as a function of F_{red} of >28,600 individual cells from one cell-culture dish transfected with rArc or rASAP expression vectors, extracted with the method described in **a**. Dashed lines indicate lower and upper gates used for subsequent data analysis. **c** Probability density of fluorescence ratio ($F_{\text{green}}/F_{\text{red}}$) of gated data from **(b)**. **d** Boxplots of $F_{\text{green}}/F_{\text{red}}$ values from three separate culture dishes of HEK293T cells expressing rArc or rASAP. **e** $F_{\text{green}}/F_{\text{red}}$ distribution of cells from independent cell-culture dishes expressing rASAP with (purple) or without (red) the ionophore gramicidin (1 μM). The $\log(F_{\text{green}}/F_{\text{red}})$ distributions were fit with Gaussian functions (solid curves, Eq. 4). **f** Median $F_{\text{green}}/F_{\text{red}}$ values from three separate cell-culture dishes (as in **(e)**). Black rhombi are mean values of the median $F_{\text{green}}/F_{\text{red}}$ values from individual dishes. **g** Normalized $F_{\text{green}}/F_{\text{red}}(V_m)$ of rASAP with superimposed Boltzmann-type functions (Eq. 1) (from Fig. 1f); parameters of the fit were $R_{\text{max}} = 0.56$, $\Delta_r = -178.6\%$, $V_{\text{half}} = -11.5 \text{ mV}$, $k_s = 54.0 \text{ mV}$. Average V_m of HEK293T cells (red) was estimated by normalization of $F_{\text{green}}/F_{\text{red}}$ of untreated cells to $F_{\text{green}}/F_{\text{red}}$ of gramicidin-treated cells, assuming full depolarization to 0 mV by gramicidin. Each data point is the average of 3 individual measurements (as in **(e, f)**).

distribution of $F_{\text{green}}/F_{\text{red}}$, was 1% for rASAP (Fig. 2e), i.e. smaller than the symbol size in Fig. 2f. To estimate the dish-to-dish variation, we measured cells expressing rASAP on five independent days with three dishes each and achieved an average standard deviation of the median $F_{\text{green}}/F_{\text{red}}$ from dish to dish of $1.8 \pm 0.3\%$.

To derive a rough estimate of the average V_m of the cell population based on the medians of the $F_{\text{green}}/F_{\text{red}}$ signals of rASAP on a microscope without patch-clamp control, we used gramicidin, an ionophore that depolarizes cells to about 0 mV⁹. We normalized the average median $F_{\text{green}}/F_{\text{red}}$ values of three independent cell-culture dishes of untreated cells to the average $F_{\text{green}}/F_{\text{red}}$ value of three cell-culture dishes with gramicidin-treated cells on the same day (Fig. 2e–g) and used the normalized $F_{\text{green}}/F_{\text{red}}(V_m)$ from patch-clamp experiments as calibration curve (Fig. 1f). Samples with gramicidin exhibited a lower $F_{\text{green}}/F_{\text{red}}$ median value than samples without gramicidin. We repeated the measurements on five different days and found a consistent shift in the median $F_{\text{green}}/F_{\text{red}}$ value of samples treated with gramicidin by $-16.5 \pm 0.7\%$ (standard deviation of 1.4%) compared to untreated cells, indicating a stable average V_m value of the HEK293T cell populations.

Using the parameters from the patch-clamp calibration curve and the $F_{\text{green}}/F_{\text{red}}$ of gramicidin-treated cells as reference for

0 mV, we estimated an average resting V_m of about -40 mV for HEK293T cell populations, which is in good agreement with previous reports^{10,34}. Notably, the width (geometric standard deviation) of the $F_{\text{green}}/F_{\text{red}}$ distribution of gramicidin-treated cells (factor 1.36 ± 0.03 , sd) was not diminished but rather slightly increased compared to untreated cells (1.31 ± 0.01 , sd, Fig. 2e), suggesting that the cell-to-cell variation in $F_{\text{green}}/F_{\text{red}}$ is mainly related to voltage-independent variations in the recorded $F_{\text{green}}/F_{\text{red}}$ signal and thus precluding inferences about V_m of individual cells. Nevertheless, the stability and reproducibility render the median values of $F_{\text{green}}/F_{\text{red}}$ distributions as robust descriptors of V_m of large cell populations.

We also performed similar experiments with cancer cell lines derived from mouse neuroblastoma (Neuro2A) and human melanoma (A375); in both cell lines, robust expression of rASAP was observed and cell depolarization by application of gramicidin yielded shifts in the medians of the $F_{\text{green}}/F_{\text{red}}$ distributions by 16% and 23% for Neuro2A and A375 cells, respectively (Supplementary Fig. 4).

To examine if rArc and rASAP are also suited to detect physiological changes in compound resting V_m , e.g., induced by the activity of ion channels, we overexpressed the mouse inward rectifier K^+ channel Kir2.1 (mKir2.1), which stabilizes a negative V_m in excitable cells³⁵. Previous reports showed that Kir2.1 is also

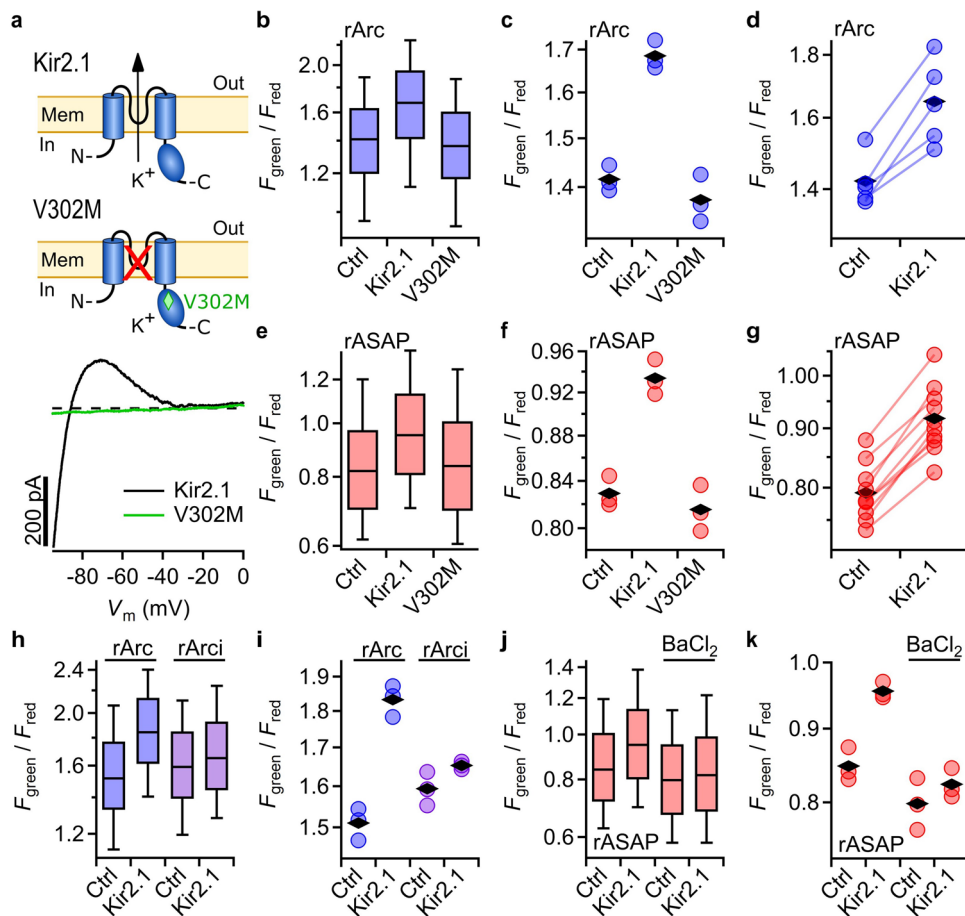


Fig. 3 Measurement of Kir2.1-induced HEK293T cell hyperpolarization. **a** Schematics of one of four subunits forming a functional inward rectifier K⁺ channel Kir2.1 or the nonconducting variant V302M, which causes the Andersen-Tawil syndrome; bottom, representative current traces as function voltage for mouse Kir2.1 (black) or variant V302M (green), expressed in HEK293T and recorded in whole-cell patch-clamp configuration. Dashed line indicates zero current level. **b** Boxplots of $F_{\text{green}}/F_{\text{red}}$ from images of HEK293T cells expressing rArc alone (Ctrl) or coexpressing Kir2.1 or Kir2.1-V302M. **c** Median ratio values of three independent samples measured on the same day; black rhombi indicate means of the median values. **d** $F_{\text{green}}/F_{\text{red}}$ from samples with rArc (Ctrl) or rArc-Kir2.1 from five different measurement days. Each data point is the mean of at least three individual median measurements (as in **b**, **c**). Data points connected by lines were acquired on the same day. **e-g** As in (**b-d**) but with cells coexpressing rASAP; from 10 days in (**g**). **h** Boxplots of $F_{\text{green}}/F_{\text{red}}$ from cells expressing rArc or rArci, a rArc variant with reduced voltage sensitivity (Supplementary Fig. 6), with and without Kir2.1 and (**i**) median values of three separate samples. **j** Boxplots of $F_{\text{green}}/F_{\text{red}}$ of cells expressing rASAP alone or coexpressing mKir2.1 with or without the mKir2.1 blocker BaCl₂ (1 mM) and **k**, median ratio values of three independent samples.

capable of hyperpolarizing HEK293T cells in a physiological saline solution¹⁶. To exclude the possibility of a nonspecific interference of the channel proteins with the GEVIs, we also expressed variant Kir2.1-V302M. This mutation causes the Andersen-Tawil syndrome in humans and abolishes the ion conduction without influencing the channel's plasma membrane localization³⁵. Whole-cell patch-clamp recordings confirmed the strong inwardly rectifying K⁺ current of the wild-type channel and lack of current for the Andersen-Tawil mutant (Fig. 3a).

For rArc and rASAP, F_{green} alone failed to show systematic changes in response to mKir2.1 expression (Supplementary Fig. 5). In contrast, the ratio of F_{green} and F_{red} of cells expressing mKir2.1 was elevated in every experiment on every measurement day for rArc (Fig. 3b-d) as well as for rASAP (Fig. 3e-g), justifying the ratiometric approach in rArc and rASAP to compensate for variations in GEVI expression intensity. We observed an increase of the median $F_{\text{green}}/F_{\text{red}}$ by Kir2.1 overexpression of $16.1 \pm 2.6\%$ (from 5 days) for rArc and $15.9 \pm 1.2\%$ (from 10 days) for rASAP. Cells expressing the non-conducting variant Kir2.1-V302M yielded $F_{\text{green}}/F_{\text{red}}$ values similar to those in control cells for both sensor types.

Since $F_{\text{green}}/F_{\text{red}}$ of rArc strongly depended on pH_i, we also generated rArci, a rArc variant with charge neutralizing mutations in the voltage-sensing domain, which were shown to be involved in voltage-sensor movement³⁶. As expected, rArci had a markedly decreased voltage sensitivity but an almost unaltered pH_i sensitivity of the $F_{\text{green}}/F_{\text{red}}$ signal (Supplementary Fig. 6) and, thus, served as a pH_i control. The increase in $F_{\text{green}}/F_{\text{red}}$ of rArc in cells overexpressing Kir2.1 was strongly diminished in rArci (Fig. 3h, i), indicating that the observed signal change in rArc due to Kir2.1 overexpression was mainly caused by a change in V_m and not in pH_i. To independently validate that it is the ion conduction through Kir2.1 that leads to hyperpolarization, we treated cells with the Kir2.1 blocker Ba²⁺. BaCl₂ decreased rASAP $F_{\text{green}}/F_{\text{red}}$ to levels similar to those found in cells without Kir2.1 (Fig. 3j, k), demonstrating that the observed hyperpolarization is caused by Kir2.1 channel activity.

In conclusion, both rArc and rASAP, in combination with the assays described, are capable of resolving differences in resting V_m of different cell groups induced by physiological stimuli. Because of the higher dynamic range and pH_i stability, we performed further experiments exclusively with rASAP.

Impact of voltage-gated K⁺ channels on cellular resting V_m. Various cancer cell types possess markedly upregulated levels of K⁺ channels which can promote hyperpolarization¹. For example, the voltage-gated K⁺ channel K_V10.1 (ether à go-go 1, EAG1, *KCNH1*) was found overexpressed in 80% of biopsies from the most common solid tumors⁴. The large-conductance voltage- and Ca²⁺-activated K⁺ channel Slo1 (BK, *KCNMA1*) was found upregulated in prostate cancer cells². Furthermore, gain-of-function mutations of K_V10.1 are associated with severe genetic diseases, such as the autosomal dominant Temple-Baraitser syndrome and other developmental disorders causing dysmorphic physical features⁶. The mechanisms underlying these pathophysiological processes may be related to changes in resting V_m of cells expressing these channels. Because channel open probabilities of Slo1 and K_V10.1 are strongly affected by intracellular factors such as Ca²⁺, Mg²⁺, or pH_i^{37–39}, the channels' impact on cellular V_m under resting conditions is hardly accessible with standard electrophysiological methods.

We investigated the impact of K_V10.1 channels and the Temple-Baraitser mutation K_V10.1-K217N on V_m in HEK293T cells (Fig. 4). While a gain-of-function phenotype of this mutation has been described⁶, the impact on V_m has not been experimentally addressed. Robust functional expression of wild-type and K_V10.1-K217N channels was electrophysiologically confirmed (Fig. 4b, c). At negative voltages, cells expressing the variant K217N exhibited greater outward currents than those with wild-type channels (Fig. 4c), suggesting that the K217N variant is capable of hyperpolarizing the cells. The cells expressing wild-type K_V10.1 had a modestly greater $F_{\text{green}}/F_{\text{red}}$ of $3.7 \pm 1.9\%$ (from 3 days) compared with cells without ectopic channel expression (Fig. 4d, e). Cells expressing the Temple-Baraitser mutant K217N showed a greater change in the fluorescence ratio signal of $12.7 \pm 2.2\%$ (from 3 days) over control cells (Fig. 4d, e). This greater hyperpolarization by K_V10.1-K217N is in good agreement with the electrophysiological results obtained in individual cells (Fig. 4b, c).

The impact of K_V10.1-K217N on V_m of HEK293T cells was pronounced and readily measured with this approach. The increase in $F_{\text{green}}/F_{\text{red}}$ of wild-type K_V10.1 expressing cells compared with cells expressing only rASAP, however, was small and not seen on every day (3 out of 5 days). A potential confounding factor could be the selection of the host cells. For example, the observed day-to-day variation in K_V10.1-induced hyperpolarization is expected because HEK293T cells are electrically coupled¹⁰ and therefore may depend on variations in cell density and transfection efficiency. Endogenous Cl⁻ channels, such as VRAC Cl⁻ channels that are expressed in HEK293T cells⁴⁰, may furthermore counteract cell hyperpolarization by K_V10.1. This notion is supported by experiments with the Cl⁻ channel blocker DCPIB. DCPIB lowered $F_{\text{green}}/F_{\text{red}}$ compared to the control cells, while it increased $F_{\text{green}}/F_{\text{red}}$ in cells expressing K_V10.1 (Fig. 4f, g). Independent measurements on 3 different days revealed that application of 10 μM DCPIB increased the average change in $F_{\text{green}}/F_{\text{red}}$ of K_V10.1-expressing cells over control cells to $6.8 \pm 1.1\%$ (Fig. 4h). DCPIB thus eliminated part of the shunting effect of background Cl⁻ conductance and enhanced the resolution of the impact of K_V10.1 expression.

Overexpression of pore-forming human Slo1 (hSlo1) subunits of large-conductance Ca²⁺- and voltage-dependent BK channels did not change rASAP's $F_{\text{green}}/F_{\text{red}}$ signal, consistent with these channels being mostly closed near resting V_m. However, hSlo1 variants with the voltage dependence of opening shifted in the negative direction did increase $F_{\text{green}}/F_{\text{red}}$ commensurate with their electrophysiological properties (Supplementary Fig. 7).

Monitoring of functional ion channel biogenesis under live-cell culture conditions. Processes that involve altered expression of ion channels, transporters, and pumps can occur on timescales of minutes to several hours. Detecting the impact on V_m of such slow events requires a sensor that is stable under cell-culture conditions for the respective durations. Ratiometric GEVIs may be suited for this purpose because the ratioing should compensate variations in GEVI expression levels.

As a proof of concept, we measured the $F_{\text{green}}/F_{\text{red}}$ dynamics following the induced expression of Kir2.1 channels in real time over many hours. We designed an expression vector (pDox) based on the TetOn 3G system⁴¹, allowing the doxycycline-induced expression of Kir2.1 channels (Fig. 5a). Control experiments using the same vector system expressing mCherry showed an up to 650-fold increase in F_{red} by doxycycline 24 h after induction (Supplementary Fig. 8a, b). A weak basal leak transactivation was seen also in the absence of doxycycline. Accordingly, cells transfected with rASAP and Kir2.1 in the pDox vector showed slightly elevated $F_{\text{green}}/F_{\text{red}}$ values compared with cells transfected with rASAP and the empty pDox vector (Supplementary Fig. 8c).

Because the cell-culture medium dedicated for live-cell imaging (FluoroBrite DMEM + 10% FCS) exhibited strong green background fluorescence, we bleached the medium for 3 h with 470-nm light before use (Supplementary Fig. 9a, b). The bleached medium by itself neither altered the cell number nor rASAP's $F_{\text{green}}/F_{\text{red}}$ of the transfected cells compared to non-bleached medium (Supplementary Fig. 9c–e). We did not use Hoechst 33342 for nuclei identification in long-term live-cell imaging experiments because of its previously reported phototoxicity under repeated illumination³³; instead, the F_{red} and F_{green} was integrated for all pixels with F_{red} counts between 500 and 3500. Each cell sample was characterized by the mean $F_{\text{green}}/F_{\text{red}}$ (\pm sem) of four images at different locations in one cell-culture dish.

HEK293T cells were transfected with rASAP and Kir2.1 in pDox or rASAP and empty pDox vectors (Ctrl). Consistent with the basal transactivation activity of the pDox vector, $F_{\text{green}}/F_{\text{red}}$ values in the cells transfected with Kir2.1 expression vector were already elevated compared to control cells before application of doxycycline (compare circles with triangles in Fig. 5b). After an initial transient in $F_{\text{green}}/F_{\text{red}}$ of about two sample points for all cell samples—presumably caused by opening the incubation chamber and mixing the cell-culture media—only the cells with the Kir2.1 expression vector and doxycycline application showed delayed increase in $F_{\text{green}}/F_{\text{red}}$ over the empty vector controls (Fig. 5b, c), indicating cell hyperpolarization via doxycycline-induced increase in Kir2.1 protein production. The change of around 8% over empty control vector (Fig. 5c) was smaller than in the high-content assay described above (15.9%, Fig. 3g). This is likely attributed to the analysis method, which integrates the signal from the whole cells including GEVI signal originating from non-responsive parts of the cells such as Golgi and ER. The time course of $F_{\text{green}}/F_{\text{red}}$ followed a sigmoidal saturating function, reaching a half-maximal change in $F_{\text{green}}/F_{\text{red}}$ after about 73 min with an increase from 20 to 80% within 34 min (Fig. 5c). The initial delay in the change in $F_{\text{green}}/F_{\text{red}}$ of about 40–50 min provides an estimate of the minimum biogenesis latency of functional Kir2.1 channels in HEK293T cells, including induction of transcription, translation, subunit assembly, and membrane trafficking.

Discussion

The ratiometric genetically encoded voltage indicators rArc and rASAP were developed for comparison of resting V_m of different

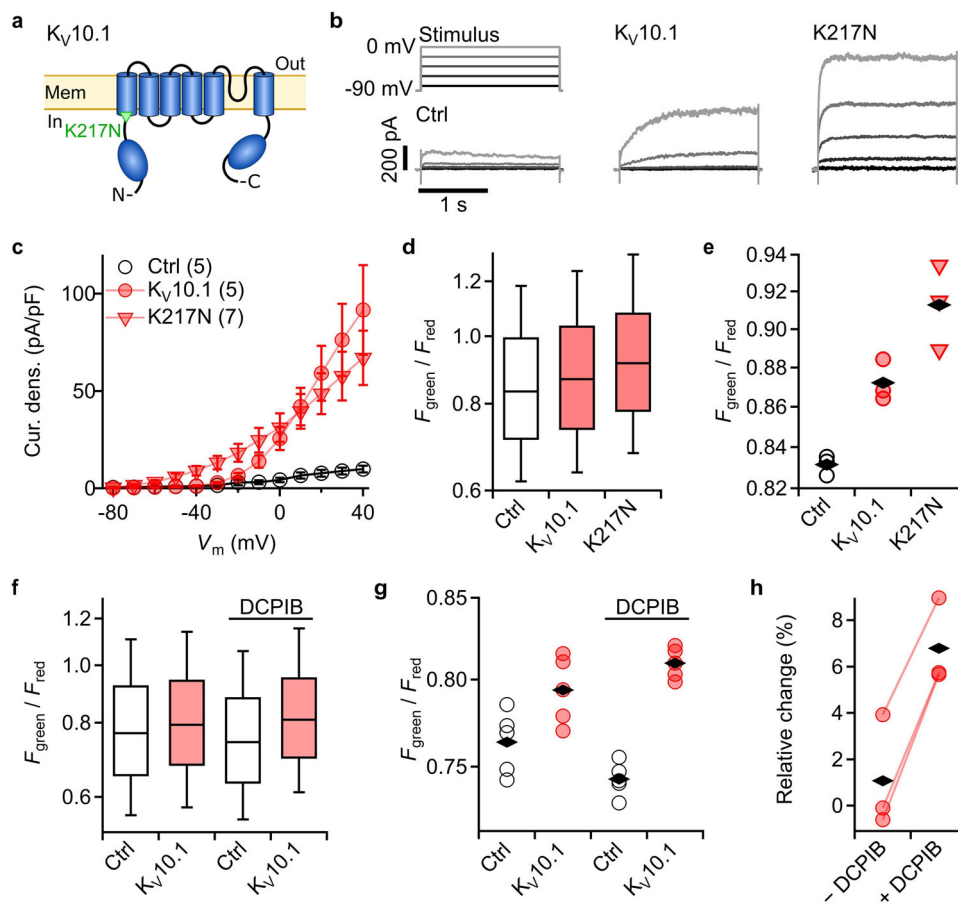


Fig. 4 **Kv10.1-K217N, a causative mutation for Temple-Baraitser syndrome, strongly hyperpolarizes HEK293T cells.** **a** Schematic of one of four subunits forming a functional human ether à go-go channel (Kv10.1). Point mutation K217N shifts the current-voltage relationship to more negative voltages. **b** Representative current traces of HEK293T cells expressing rASAP alone (Ctrl) or coexpressing Kv10.1 or Kv10.1-K217N. Current traces were acquired using the depicted voltage pulse protocol. Control recordings were acquired from cells without Kv10.1. **c** Current density as a function of the voltage of cells expressing rASAP alone or coexpressing the indicated Kv10.1 variant. Data points are means \pm sem, n is given in parentheses. Straight lines connect data points for clarity. **d** Boxplots of $F_{\text{green}}/F_{\text{red}}$ from HEK293T cells expressing rASAP alone or coexpressing the indicated variant. **e** Median ratio values of three independent samples (as in **d**) measured on the same day; black rhombi are average values; cells >4400 for each measurement. **f** $F_{\text{green}}/F_{\text{red}}$ of cells expressing Kv10.1 with and without $10\ \mu\text{M}$ of the Cl^- channel blocker DCPIB. **g** Median ratio values of five independent samples (as in **f**). **h** Relative change in $F_{\text{green}}/F_{\text{red}}$ of cells with Kv10.1 over control cells with and without DCPIB from three days; connected data points are average changes acquired on the same day.

cell groups. rASAP is preferred over rArc based on faster kinetics, pH_i stability, and larger dynamic range. With a change in fluorescence-intensity ratio of about 44% in the physiological V_m range between -100 and 60 mV, rASAP is well suited to resolve both hyperpolarizing and depolarizing events. The high-content workflow protocol (Fig. 2a) allows to detect long-term changes in compound resting V_m in non-excitable cells caused by overexpression of various K^+ channel types. The impacts of these channels on the $F_{\text{green}}/F_{\text{red}}$ values of rASAP are nicely commensurate with the electrophysiological characteristics of the channels. The developed approach, therefore, allows to survey the phenotypes of channel mutants with high throughput without electrode-based electrophysiology. Due to its less invasive nature compared to electrode-based methods, the optical approach allows to compare compound resting V_m under physiological conditions. Furthermore, ratiometric GEVIs are suited to track the kinetics of functional ion channel biogenesis in real time, which had not been previously achieved. Using rASAP, we estimate the latency for an impact on V_m by the appearance of functional Kir2.1 channels in the plasma membrane, including induction of transactivation, transcription, translation, subunit assembly, and membrane trafficking, to be about 40–50 min.

With the developed techniques, compound resting V_m of different cell populations are reliably compared, but the calibration of the automatically acquired signals requires care. Based on calibration parameters derived from patch-clamp experiments with manually selected ROIs encompassing cell edges only, we estimated a resting V_m in HEK293T cells of roughly -40 mV, similar to those in other studies^{10,34}. Assuming a constant V_m of -40 mV for control HEK293T cells, the estimated V_m in cells overexpressing Kir2.1 was -95 mV, which is compatible with the equilibrium potential for K^+ (Fig. 3a), between -90 and -100 mV under live-cell conditions (Supplementary Fig. 10), and Kir2.1 being the major determinant for V_m under this condition. However, the calculated absolute V_m values must be interpreted cautiously because the calibration strongly depends on the area of ROI selection and the amount of unresponsive intracellular fractions of the GEVI signal (Supplementary Fig. 10). We observed that the automatic analysis procedure detecting the cell nucleus mainly uses signal of defocused membrane regions from above and below the nucleus and largely excludes areas in the cell with especially bright intracellular structures, which are likely originating from GEVI signal in Golgi (Fig. 2a). In addition, the stringent upper limit removes cells with strongly overexpressed

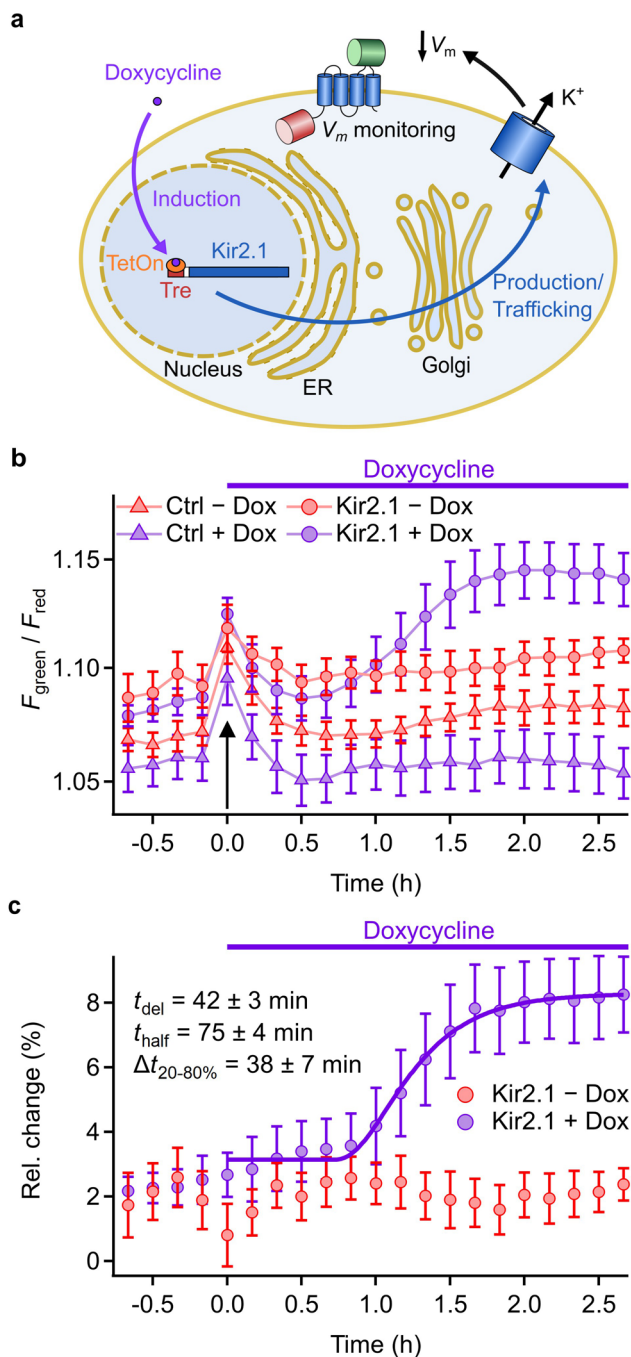


Fig. 5 Time course of cell hyperpolarization induced by triggered expression of Kir2.1. **a** Schematic of measurement of production speed of functional Kir2.1 channels using ratiometric GEVIs as V_m monitor. GEVIs are constitutively produced from an expression vector with CMV promoter. Kir2.1 expression is controlled by the Tre/TetOn system, which is triggered by the application of doxycycline. **b** Time course of F_{green}/F_{red} of HEK293T cells transfected with rASAP and a doxycycline-inducible expression vector system. Gene expression of Kir2.1 or Ctrl (empty pDox vector) with 200 ng/ml doxycycline (Dox) was induced as indicated (purple symbols). Application of solution induced a transient increase of F_{green}/F_{red} in all samples (black arrow). Under control conditions (red symbols), the same application handling was performed without Dox. Images were acquired every 10 min. DMEM-F12 cell culture medium was exchanged with FluoroBrite DMEM 13 h before doxycycline application. Values are means \pm sem of images from four different locations in one cell-culture dish. **c** Relative change in F_{green}/F_{red} , normalized to the respective control, as a function of time. The solid curve for the Dox-induced data is a fit according to Eq. 5, resulting in 5.1% maximal relative change and the indicated kinetic parameters.

also applicable for existing and future ratiometric GEVIs. Single-cell V_m accuracy of future ratiometric GEVIs not only requires improvements in Δr but also in plasma membrane trafficking²³. Furthermore, a single fluorescence component that already provides a ratiometric signal, as in the ratiometric Ca^{2+} indicator ratio pericam⁴², may be beneficial.

Using our newly developed tools we observed that Kv10.1 channels, which are upregulated in 80% of the most common solid tumors⁴, mildly hyperpolarize HEK293T cells when ectopically expressed. The mutation K217N in Kv10.1, which causes severe developmental defects as observed in Temple-Baraitser syndrome patients⁶, shifts average V_m by roughly -40 mV compared to control HEK293T cells, consistent with the electrophysiological data (Fig. 4; Supplementary Fig. 10). The developmental defects observed in Temple-Baraitser syndrome therefore may be caused by hyperpolarization of mesenchymal stem cells, where Kv10.1 channels are reported to influence cell proliferation and differentiation⁸. Missense mutations leading to complex developmental phenotypes have been associated with various K^+ channel genes and many of the mutations increase channel activity. However, the underlying mechanisms are poorly understood³. Long-lasting cell hyperpolarization may be a common feature for some of the disease-causing mutations including mutants of *KCNJ2*, *KCNJ6*, *KCNJ8*, and *KCNN3*³. Studying such mutants with the devised methods for their impact on V_m will advance our knowledge on mechanistic roots of such developmental diseases and the underlying regulatory processes.

An important prerequisite to a wide application is the feasibility of applying rASAP in various cell types. As indicated in Supplementary Fig. 4, voltage-dependent rASAP signals are readily detectable in the neuroblastoma and melanoma cells examined. Since the fraction of V_m -responsive and V_m -unresponsive components of GEVI fluorescence may vary between different cell types, cell-specific calibration is required.

In conclusion, the ratiometric V_m sensors and the data acquisition and analysis techniques described here are well suited for detecting differences in compound V_m among independent cell groups in the whole physiological voltage range and represent a useful set of tools for studying disease-relevant ion channels and variants. The methodologies are applicable for high-throughput ion channel drug screening and should facilitate our understanding of the roles of resting V_m in fundamental processes such as ion channel biogenesis, transmembrane transport, cell cycle progression, and cancer.

GEVI and thus especially poor membrane trafficking (Fig. 2a, b, Supplementary Fig. 11). Both factors together may explain the unexpectedly good outcome of the automated analysis procedure.

The broad cell-to-cell variation of the F_{green}/F_{red} signal of all developed GEVIs may appear to suggest a large V_m heterogeneity. However, the F_{green}/F_{red} distribution did not sharpen with gramicidin application, which should bring all cells close to 0 mV and therefore eliminate large V_m variations among cells. Therefore, the cell-to-cell variation seems to be mainly related to V_m -independent variations of F_{green}/F_{red} , which might be caused by factors as imperfect trafficking as well as differential maturation, degradation, and sensitivity to pH_i and the cellular redox state of the two fluorescent components of the sensor. While the broad cell-to-cell variation does not offer single-cell V_m accuracy, the developed high-content methods clearly allow to detect difference in average resting V_m among independent cell groups and will be

Methods

Molecular biology. rArc and rASAP variants were constructed with standard molecular biology methods. Construction of rArc-mCherry: mCherry from pmCherry_C2, extracted with *NheI* and *EcoRI*, was combined with PCR-amplified ArcLightQ239 (36856, Addgene), flanked by *EcoRI* and *NotI* restriction sites in pcDNA3.1(+), cut with *NheI* and *NotI* (NEB, Ipswich, Massachusetts, USA). rArc-mCherry-M71T was generated by site-directed mutagenesis of mCherry in rArc-mCherry. Analogously, rArc was generated by exchanging mCherry with PCR-amplified mKate2 from heme sensor 1 (159169, Addgene, Watertown, Massachusetts, USA) using flanking *NheI* and *EcoRI* restriction sites. rArci, a rArc variant with mutations R229Q and R232Q, was generated by site-directed mutagenesis. Construction of rASAP: ArcLightQ239 was replaced in rArc by an ASAP-coding synthetic DNA double strand (Eurofins Genomics, Luxemburg), which contained flanking *EcoRI* (5') and *NotI* (3') sites. Our version of ASAP contained the R415Q mutation of ASAP2s, I67T, and Q397R, which reversed the point mutation introduced in ASAP1²⁸. For rASAP-al, the linker between segment S3 and the cpGFP domain of rASAP was exchanged according to Fig. 1b¹⁶.

For the generation of coexpression vectors, the Kan/Neo gene of pcDNA3.1(+)⁴ was replaced with the coding sequences of the K⁺ channels human Slo1 (BK, KCNMA1, NP_002238.2), human Kv10.1 (hEAG1, KCNH1, NP_002229.1), or mouse Kir2.1 (*Kcnj2*, NP_032451.1). Point mutations were introduced by site-directed mutagenesis.

The doxycycline-inducible vector (here called pDox) was generated by exchanging the CMV promoter of pcDNA3.1(+)⁴ with the TRE3G promoter and the Kan/Neo cassette with the coding sequence for the TetOn3G gene, of pHRE-F1Alpha-puro-T2A-Tet-on 3G-TRE3G-Ascl1 (118593, Addgene). For inducible expression of Kir2.1 or mCherry, the corresponding genes were placed in the multiple-cloning site of the pDox vector following the Tre promoter. All clones were verified with DNA sequencing (Eurofins Genomics). Sequences of plasmids used in this study are available as supplementary information files (Supplementary Data 3).

Cell culture. Human embryonic kidney 293T cells (HEK293T; CAMR, Porton Down, Salisbury, UK) were cultured in 1:1 Dulbecco's Minimal Eagles Medium and Ham's F12 medium (DMEM-F12, Thermo Fisher Scientific, Waltham, Massachusetts, USA) supplemented with 10% fetal bovine serum in a humidified incubator at 37 °C with 5% CO₂. Mouse neuroblastoma Neuro2A cells (DSMZ, Braunschweig, Germany) were cultured in Minimal Eagles Medium (MEM, Sigma Aldrich) and human melanoma A375 cells (ATCC, Manassas, VA, USA) were cultured in DMEM (Sigma Aldrich) with 10% fetal bovine serum (FCS) in a humidified incubator at 37 °C with 10% CO₂.

For electrophysiological, high-content, and long-term live-cell imaging experiments, cells were plated on 35-mm glass-bottom dishes (Ibidi, Martinsried, Germany) at ≈20,000 cells/dish. One day after plating, HEK293T and Neuro2A cells were transfected with plasmids using the Roti[®]-fect transfection kit (Carl Roth, Karlsruhe, Germany) with 1 μg DNA per glass-bottom dish. A375 cells were electroporated (4D-Nucleofector, Lonza, Basel, Switzerland) with 1.5 μg DNA using the SF Cell Line 4D-Nucleofector kit (Lonza) according to the supplier instructions.

Electrophysiological and high-content recordings were performed two days after transfection for HEK293T cells and one day after transfection for Neuro2A and A375 cells.

Imaging and photometry under electrophysiological control. Combined electrophysiological and imaging recordings (Supplementary Fig. 1) were performed on an Axio Observer inverted microscope equipped with the Colibri-2 LED illumination system (Carl Zeiss, Jena, Germany) and an EC-Plan Neofluar oil 40× objective (NA 1.3, Zeiss). Images were acquired with a CMOS camera (ORCA-Flash 4.0 Digital Camera C11440, Hamamatsu, Japan) operated with SmartLux software (HEKA Elektronik, Lambrecht, Germany). Electrophysiological measurements were performed with an EPC10 double patch-clamp amplifier controlled by PatchMaster software (HEKA Elektronik). The following excitation light sources were used: 470-nm LED (BP 460/50) for ASAP and ArcLight, 530-nm LED (BP 545/40) for mCherry and mKate2. Excitation and emission light were passed through an EGFP/mCherry (59022 Chroma) dual-emission filter set.

For experiments requiring high temporal resolution (Supplementary Fig. 2), patch clamp was combined with photometry. Light from a 470-nm LED (M470L1, Thorlabs), an EC-Plan Neofluar oil-immersion 40× objective (1.3 NA, Zeiss), and an EGFP/mCherry dual-emission filter were used. Emitted light was measured with a photodiode (FDU photodiode with view finder, T.I.L.L. Photonics, Gräfelfing, Germany) and recorded with PatchMaster (HEKA Elektronik).

Patch-clamp pipettes were fabricated from borosilicate glass, coated with dental wax and fire polished to resistances of 1–2 MΩ. Prior to recordings, the cell culture medium was removed from cells and exchanged with external solution containing (in mM) 146 NaCl, 4 KCl, 2 CaCl₂, 2 MgCl₂, and 10 HEPES (adjusted with NaOH to pH 7.4 at 22 °C). The pipette solution contained (in mM) 130 KCl, 2.5 MgCl₂, 10 ethylene glycol tetraacetic acid (EGTA), and was adjusted to pH 6.9, 7.4, or 7.9 at 22 °C with KOH. Currents were low-pass filtered at 5 kHz and sampled at 20 kHz.

Live-cell fluorescence imaging. Imaging experiments were performed on an Eclipse-Ti fluorescence microscope equipped with a DS-Qi2 camera (14 bit; Nikon, Tokyo, Japan) and a X-Cite 120 LED light source (Excelitas Technologies, Waltham, Massachusetts, USA), all controlled by the NIS4.6 software (Nikon).

The temperature of the incubation chamber (Oko Lab, Pozzuoli, Italy) was adjusted to 37 °C before the start of the measurement. Before measurements, cell culture medium was removed, the cells were washed once with 1 ml measurement buffer (see external solution for patch-clamp experiments), and subsequently the medium was replaced with 2 ml measurement buffer supplemented with 5 mM glucose and 10 μg/ml Hoechst 33342 (Invitrogen). Cells were then incubated for 30 min at 37 °C and 5% CO₂ before image acquisition. BaCl₂ was dissolved in the measurement buffer. Gramicidin D (G5002, Sigma-Aldrich) was dissolved at 2 mM in ethanol and diluted to 1 μM in measurement buffer immediately before experiments. DCPiB (4-(2-butyl-6,7-dichloro-2-cylopropyl-indan-1-on-5-yl) oxobutyric acid (Cruz Chem, Santa Cruz Biotechnology, Santa Cruz, CA, USA) was dissolved at 10 mM in DMSO and diluted to 10 μM in measurement buffer immediately before use.

For every 35-mm glass-bottom dish, images from 16 spots were acquired using a 10× objective (Plan Apo λ, NA 0.45, Nikon) and an automated stage (H117 stage with a Proscan III controller; Prior Scientific, Cambridge, UK) controlled by the NIS 4.6 (Nikon) software, avoiding an overlap of illuminated areas. The z-focus was stabilized with the Nikon Perfect Focusing System. Four images were taken with blue excitation (GFP-3035D-000, 0.5 or 1.0 s exposure time each with a camera gain factor of 5.1) and one with green excitation (4040C-000 BrightLine, 0.5 or 1.0 s exposure time, with a camera gain factor of 5.1). The Hoechst 33342 signal was recorded with UV excitation (DAPI-50LP-A-000, 3 ms; filter sets from Semrock, Rochester, NY, USA). In addition, one image was acquired in transmission mode.

For real-time live-cell experiments, DMEM-F12 was replaced with FluoroBrite DMEM medium (Thermo Fisher Scientific) supplemented with 10% FCS 24 h after transfection; the medium was bleached for 3 h with a 470 nm LED (100%, M470L1, Thorlabs) before usage (Supplementary Fig. 9). For induction of gene expression from pDox, the medium was supplemented with 200 ng/ml doxycycline hyclate dissolved at 1 mg/ml in water (Sigma-Aldrich). Recordings were performed in a humidified atmosphere at 37 °C and 5% CO₂. To minimize photobleaching, one green and one red image (200 ms exposure each, camera gain factor of 13.9) were acquired every 10 min.

Automated image analysis. Image analysis was performed with Fiji software⁴³. For high-content imaging, the camera offset for each channel was subtracted; the background of each image was subtracted individually using the built-in rolling-ball algorithm (radius of 146 μm). Subsequently, cell nuclei were detected in the Hoechst 33342/blue channel by converting the image into a binary mask with a manually set threshold. The built-in watershed algorithm was then used to separate nuclei that were too close to be separated via thresholding. Using the particle analysis tool of Fiji, individual nuclei were detected for each image. Particles crossing the edge of the image, as well as particles of unreasonable size (<26 μm² and >117 μm²) were excluded. ROIs were automatically drawn at the boundary of each particle, and fluorescence parameters were extracted for each individual cell for the green, red, and blue channels. For the green channel, only the fourth image was used for analysis in order to measure F_{green} after complete photoswitching (Supplementary Fig. 1a). A schematic illustration of the analysis procedure is shown in Fig. 2a. Compiled data were further analyzed with Igor Pro 8 (WaveMetrics, Lake Oswego, OR, USA).

Several measures were applied to avoid bias due to technical limitations. First and foremost, the limited dynamic range of the recording camera defines an upper limit for strongly expressing cells and high $F_{\text{green}}/F_{\text{red}}$ values, which systematically excludes high $F_{\text{green}}/F_{\text{red}}$ values (Supplementary Fig. 11). Thus, cells with very high F_{red} signals were excluded from analysis (Fig. 2b). Second, insufficient background subtraction can result in systematic, expression-dependent changes in $F_{\text{green}}/F_{\text{red}}$. This problem was especially conspicuous for F_{green} when the strongly auto-fluorescent cell culture medium (DMEM-F12) was not completely removed (Supplementary Fig. 12). Therefore, the median $F_{\text{green}}/F_{\text{red}}$ values as a function of F_{red} were plotted and a linear fit was used to determine the minimum of the squared slope (slope²) as a function of background F_{green} (Supplementary Fig. 12). In addition, cells with low F_{red} intensities, for which the error in background subtraction was largest, were excluded. The remaining cells were gated according to the cell-cycle stage: cells in the G0/G1, S, and G2/M phase were used for analysis, while cells with signals below the G0/G1 peak were considered as debris, and cells above the G2/M peaks as non-separated doublet signals.

For live-cell real-time experiments the image background for both channels was subtracted with the built-in rolling-ball algorithm. The reported phototoxicity of Hoechst 33342 under repeated illumination³³ excluded its use for long-term experiments. Instead, we used the F_{red} signal for generating a binary mask (500 counts < F_{red} < 3500 counts) and exported the average F_{green} and F_{red} values from the selected area of each image.

Fluorescence ratio- V_m curves were fit according to the following Boltzmann-type function:

$$\frac{F_{\text{green}}}{F_{\text{red}}}(V_m) = R_{\text{max}} \left\{ 1 - \frac{\Delta r/100}{1 + e^{-(V_m - V_{\text{half}})/k_r}} \right\} \quad (1)$$

with the maximum fluorescence ratio R_{\max} , the maximal relative change in ratio (Δr , in %), the voltage of half-maximal fluorescence change, V_{half} and k_s characterizing the steepness.

Kinetics of fluorescence change by voltage steps were analyzed with double-exponential fits:

$$\frac{F_{\text{green}}}{F_{\text{max}}}(t) = 1 - \frac{\Delta r}{100} [a_{\text{fast}}(1 - e^{-t/\tau_{\text{fast}}}) + a_{\text{slow}}(1 - e^{-t/\tau_{\text{slow}}})] \quad (2)$$

with the relative amplitudes $a_{\text{fast}} + a_{\text{slow}} = 1$ and the time constants τ_{fast} and τ_{slow} .

Potassium equilibrium potential (E_K) was calculated according to the Nernst equation:

$$E_K = \frac{RT}{F} \ln \left(\frac{[K^+]_{\text{out}}}{[K^+]_{\text{in}}} \right) \quad (3)$$

with $R = 8.314 \text{ J K}^{-1} \text{ mol}^{-1}$, $T = 310.15 \text{ K}$ and $F = 96,485 \text{ C mol}^{-1}$; $[K^+]_{\text{in}}$ and $[K^+]_{\text{out}}$ are internal and external K^+ concentrations, respectively.

Frequency distributions of $x = \log(F_{\text{green}}/F_{\text{red}})$ were described with Gaussian functions:

$$f(x) = f_{\text{max}} e^{-\frac{(x-x_0)^2}{2\sigma^2}} \quad (4)$$

with the maximal amplitude f_{max} , the center of the distribution x_0 , and the standard deviation σ .

The time course in $F_{\text{green}}/F_{\text{red}}$ following the induced production of ion channels was fit with a sigmoidal function for $t > 0$, from which the time at half-maximal change and the time for 20–80% change were analytically derived:

$$\frac{F_{\text{green}}}{F_{\text{red}}}(t) = y_0 + (y_{\text{max}} - y_0) \left(1 - e^{-(t-t_{\text{del}})/\tau} \right)^3 \quad (5)$$

with initial offset y_0 , the maximal relative ratio y_{max} , an initial delay t_{del} , and a time constant τ .

Statistics and reproducibility. Data are typically depicted as means \pm sem or median values unless stated otherwise. Boxes of boxplots feature 25/75% quantiles of the distributions, whiskers are 10/90% quantiles, and the central line is the median. The standard deviation of the median from individual $F_{\text{green}}/F_{\text{red}}$ distributions was estimated with resampling with replacement (Igor Pro 8). For small sample sizes, all individual data points are presented. The number of individual measurements is referred to as n and the number of independent replicates on different days as N .

Reporting summary. Further information on research design is available in the Nature Research Reporting Summary linked to this article.

Data availability

All data generated or analyzed during this study are included in this published article and its supplementary information files (Supplementary Data 1–2). Plasmids of the sensor constructs are available through Addgene. Any remaining information can be obtained from the corresponding author upon reasonable request.

Received: 25 March 2021; Accepted: 13 September 2021;

Published online: 07 October 2021

References

- Abdul Kadir, L., Stacey, M. & Barrett-Jolley, R. Emerging roles of the membrane potential: action beyond the action potential. *Front. Physiol.* **9** (2018).
- Gessner, G. et al. BK_{Ca} channels activating at resting potential without calcium in LNCaP prostate cancer cells. *J. Membr. Biol.* **208**, 229–240 (2005).
- Hamilton, M. J. & Suri, M. In *Advances in Genetics*, Vol. 105. (ed. Kumar, D.) 137–174 (Academic Press, 2020).
- Hemmerlein, B. et al. Overexpression of Eag1 potassium channels in clinical tumours. *Mol. Cancer* **5**, 41 (2006).
- Lobikin, M., Chernet, B., Lobo, D. & Levin, M. Resting potential, oncogene-induced tumorigenesis, and metastasis: the bioelectric basis of cancer in vivo. *Phys. Biol.* **9**, 065002 (2012).
- Simons, C. et al. Mutations in the voltage-gated potassium channel gene KCNH1 cause Temple-Baraitser syndrome and epilepsy. *Nat. Genet.* **47**, 73–77 (2015).
- Yang, M. & Brackenbury, W. J. Membrane potential and cancer progression. *Front Physiol.* **4**, 185 (2013).
- Zhang, Y. Y. et al. BK_{Ca} and hEag1 channels regulate cell proliferation and differentiation in human bone marrow-derived mesenchymal stem cells. *J. Cell Physiol.* **229**, 202–212 (2014).
- Klapperstück, T. et al. Calibration procedures for the quantitative determination of membrane potential in human cells using anionic dyes. *Cytom. A* **83**, 612–626 (2013).
- Lazzari-Dean, J. R., Gest, A. M. & Miller, E. W. Optical estimation of absolute membrane potential using fluorescence lifetime imaging. *Elife* **8** (2019).
- Salzberg, B. M., Davila, H. V. & Cohen, L. B. Optical recording of impulses in individual neurones of an invertebrate central nervous system. *Nature* **246**, 508–509 (1973).
- Morimoto, T. et al. Voltage-sensitive oxonol dyes are novel large-conductance Ca²⁺-activated K⁺ channel activators selective for $\beta 1$ and $\beta 4$ but not for $\beta 2$ subunits. *Mol. Pharm.* **71**, 1075–1088 (2007).
- Chamberland, S. et al. Fast two-photon imaging of subcellular voltage dynamics in neuronal tissue with genetically encoded indicators. *Elife* **6**, e25690 (2017).
- Jin, L. et al. Single action potentials and subthreshold electrical events imaged in neurons with a fluorescent protein voltage probe. *Neuron* **75**, 779–785 (2012).
- St-Pierre, F. et al. High-fidelity optical reporting of neuronal electrical activity with an ultrafast fluorescent voltage sensor. *Nat. Neurosci.* **17**, 884–889 (2014).
- Villette, V. et al. Ultrafast two-photon imaging of a high-gain voltage indicator in awake behaving mice. *Cell* **179**, 1590–1608.e1523 (2019).
- Bando, Y., Sakamoto, M., Kim, S., Ayzenshtat, I. & Yuste, R. Comparative evaluation of genetically encoded voltage indicators. *Cell Rep.* **26**, 802–813.e804 (2019).
- Hochbaum, D. R. et al. All-optical electrophysiology in mammalian neurons using engineered microbial rhodopsins. *Nat. Methods* **11**, 825–833 (2014).
- Milosevic, M. M., Jang, J., McKimm, E. J., Zhu, M. H. & Antic, S. D. In vitro testing of voltage indicators: Archon1, ArcLightD, ASAP1, ASAP2s, ASAP3b, Bongwoori-Pos6, BeRST1, FlicR1, and Chi-VSPF-Butterfly. *eNeuro* **7**, ENEURO.0060-20.2020 (2020).
- Brinks, D., Klein, A. J. & Cohen, A. E. Two-photon lifetime imaging of voltage indicating proteins as a probe of absolute membrane voltage. *Biophys. J.* **109**, 914–921 (2015).
- Hou, J. H., Venkatachalam, V. & Cohen, A. E. Temporal dynamics of microbial rhodopsin fluorescence reports absolute membrane voltage. *Biophys. J.* **106**, 639–648 (2014).
- Yang, H. H. & St-Pierre, F. Genetically encoded voltage indicators: opportunities and challenges. *J. Neurosci.* **36**, 9977–9989 (2016).
- Akemann, W. et al. Imaging neural circuit dynamics with a voltage-sensitive fluorescent protein. *J. Neurophysiol.* **108**, 2323–2337 (2012).
- Lundby, A., Mutoh, H., Dimitrov, D., Akemann, W. & Knöpfel, T. Engineering of a genetically encodable fluorescent voltage sensor exploiting fast Ci-VSP voltage-sensing movements. *PLoS ONE* **3**, e2514 (2008).
- Mishina, Y., Mutoh, H., Song, C. & Knöpfel, T. Exploration of genetically encoded voltage indicators based on a chimeric voltage sensing domain. *Front. Mol. Neurosci.* **7**, 78 (2014).
- Tsutsui, H. et al. Improved detection of electrical activity with a voltage probe based on a voltage-sensing phosphatase. *J. Physiol.* **591**, 4427–4437 (2013).
- Shcherbo, D. et al. Far-red fluorescent tags for protein imaging in living tissues. *Biochem J.* **418**, 567–574 (2009).
- Yang, H. H. et al. Subcellular imaging of voltage and calcium signals reveals neural processing in vivo. *Cell* **166**, 245–257 (2016).
- Xu, F., Shi, D. Q., Lau, P. M., Lin, M. Z. & Bi, G. Q. Excitation wavelength optimization improves photostability of ASAP-family GEVIs. *Mol. Brain* **11**, 32 (2018).
- Katayama, H., Yamamoto, A., Mizushima, N., Yoshimori, T. & Miyawaki, A. GFP-like proteins stably accumulate in lysosomes. *Cell Struct. Funct.* **33**, 1–12 (2008).
- Shen, Y., Rosendale, M., Campbell, R. E. & Perrais, D. pHuji, a pH-sensitive red fluorescent protein for imaging of exo- and endocytosis. *J. Cell Biol.* **207**, 419–432 (2014).
- Han, Z. et al. Mechanistic studies of the genetically encoded fluorescent protein voltage probe ArcLight. *PLoS One* **9**, e113873 (2014).
- Purschke, M., Rubio, N., Held, K. D. & Redmond, R. W. Phototoxicity of Hoechst 33342 in time-lapse fluorescence microscopy. *Photochem. Photobiol. Sci.* **9**, 1634–1639 (2010).
- Saminathan, A. et al. A DNA-based voltmeter for organelles. *Nat. Nanotechnol.* **16**, 96–103 (2021).
- Ma, D., Tang, X. D., Rogers, T. B. & Welling, P. A. An andersen-Tawil syndrome mutation in Kir2.1 (V302M) alters the G-loop cytoplasmic K⁺ conduction pathway. *J. Biol. Chem.* **282**, 5781–5789 (2007).
- Villalba-Galea, C. A., Frezza, L., Sandtner, W. & Bezanilla, F. Sensing charges of the *Ciona intestinalis* voltage-sensing phosphatase. *J. Gen. Physiol.* **142**, 543–555 (2013).

37. Gessner, G., Rühl, P., Westerhausen, M., Hoshi, T. & Heinemann, S. H. Fe²⁺-mediated activation of BK_{Ca} channels by rapid photolysis of CORM-S1 releasing CO and Fe²⁺. *ACS Chem. Biol.* **15**, 2098–2106 (2020).
38. Hou, S., Heinemann, S. H. & Hoshi, T. Modulation of BK_{Ca} channel gating by endogenous signaling molecules. *Physiology* **24**, 26–35 (2009).
39. Schönherr, R., Löber, K. & Heinemann, S. H. Inhibition of human ether à go-go potassium channels by Ca²⁺/calmodulin. *Embo j.* **19**, 3263–3271 (2000).
40. Friard, J. et al. LRRC8/VRAC channels exhibit a noncanonical permeability to glutathione, which modulates epithelial-to-mesenchymal transition (EMT). *Cell Death Dis.* **10**, 925 (2019).
41. Das, A. T., Tenenbaum, L. & Berkhout, B. Tet-On systems for doxycycline-inducible gene expression. *Curr. Gene Ther.* **16**, 156–167 (2016).
42. Nagai, T., Sawano, A., Park, E. S. & Miyawaki, A. Circularly permuted green fluorescent proteins engineered to sense Ca²⁺. *Proc. Natl. Acad. Sci. USA.* **98**, 3197–3202 (2001).
43. Schindelin, J. et al. Fiji: an open-source platform for biological-image analysis. *Nat. Methods* **9**, 676–682 (2012).

Acknowledgements

We thank Prof. Brian Salzberg (University of Pennsylvania) for numerous discussions and critical reading of the manuscript. We thank Angela Roßner for technical support. Grant support: German Research Foundation (HE 2993/16-1 and RTG 2155). T.H. was supported in part by NIH GM121375.

Author contributions

P.R. designed and performed experiments, analyzed the data, and wrote the paper; J.M.L. and J.R. performed experiments; R.S. designed and performed experiments and revised the paper; T.H. designed experiments and revised the paper; S.H.H. supervised the project, designed experiments, and wrote the paper.

Funding

Open Access funding enabled and organized by Projekt DEAL.

Competing interests

The authors declare no competing interests.

Additional information

Supplementary information The online version contains supplementary material available at <https://doi.org/10.1038/s42003-021-02675-0>.

Correspondence and requests for materials should be addressed to Stefan H. Heinemann.

Peer review information *Communications Biology* thanks the anonymous reviewers for their contribution to the peer review of this work. Primary Handling Editors: Eliana Scemes and Anam Akhtar.

Reprints and permission information is available at <http://www.nature.com/reprints>

Publisher's note Springer Nature remains neutral with regard to jurisdictional claims in published maps and institutional affiliations.



Open Access This article is licensed under a Creative Commons Attribution 4.0 International License, which permits use, sharing, adaptation, distribution and reproduction in any medium or format, as long as you give appropriate credit to the original author(s) and the source, provide a link to the Creative Commons license, and indicate if changes were made. The images or other third party material in this article are included in the article's Creative Commons license, unless indicated otherwise in a credit line to the material. If material is not included in the article's Creative Commons license and your intended use is not permitted by statutory regulation or exceeds the permitted use, you will need to obtain permission directly from the copyright holder. To view a copy of this license, visit <http://creativecommons.org/licenses/by/4.0/>.

© The Author(s) 2021